

# Generative Models for Reproducible Coronary Calcium Scoring

Sanne G.M. van Velzen<sup>1,2,\*</sup>, Bob D. de Vos<sup>1</sup>, Julia M.H. Noothout<sup>1</sup>, Helena M. Verkooijen<sup>3</sup>,  
Max A. Viergever<sup>2</sup>, Ivana Išgum<sup>1,4,5,6</sup>

<sup>1</sup>Department of Biomedical Engineering and Physics, Amsterdam University Medical Centers - location AMC, the Netherlands

<sup>2</sup>Image Sciences Institute, Univerisity Medical Center Utrecht and Utrecht University, Utrecht, the Netherlands

<sup>3</sup>Imaging Division, Univerisity Medical Center Utrecht, Utrecht, the Netherlands

<sup>4</sup>Department of Radiology and Nuclear Medicine, Amsterdam University Medical Centers - location AMC, the Netherlands

<sup>5</sup>Amsterdam Cardiovascular Sciences, Amsterdam University Medical Centers, the Netherlands

<sup>6</sup>Informatics Institute, Faculty of Science, University of Amsterdam, the Netherlands

## Abstract.

**Purpose:** Coronary artery calcium (CAC) score, i.e. the amount of CAC quantified in CT, is a strong and independent predictor of coronary heart disease (CHD) events. However, CAC scoring suffers from limited interscan reproducibility, which is mainly due to the clinical definition requiring application of a fixed intensity level threshold for segmentation of calcifications. This limitation is especially pronounced in non-ECG-synchronized CT where lesions are more impacted by cardiac motion and partial volume effects. Therefore, we propose a CAC quantification method that does not require a threshold for segmentation of CAC. **Approach:** Our method utilizes a generative adversarial network where a CT with CAC is decomposed into an image without CAC and an image showing only CAC. The method, using a CycleGAN, was trained using 626 low-dose chest CTs and 514 radiotherapy treatment planning CTs. Interscan reproducibility was compared to clinical calcium scoring in radiotherapy treatment planning CTs of 1,662 patients, each having two scans. **Results:** A lower relative interscan difference in CAC mass was achieved by the proposed method: 47% compared to 89% manual clinical calcium scoring. The intraclass correlation coefficient of Agatston scores was 0.96 for the proposed method compared to 0.91 for automatic clinical calcium scoring. **Conclusions:** The increased interscan reproducibility achieved by our method may lead to increased reliability of CHD risk categorization and improved accuracy of CHD event prediction.

**Keywords:** Calcium scoring, Reproducibility, CT, Generative models, CycleGAN.

\*Sanne G.M. van Velzen, [s.g.m.vanvelzen@amsterdamumc.nl](mailto:s.g.m.vanvelzen@amsterdamumc.nl)

## 1 Introduction

Coronary heart disease (CHD) is among the leading causes of death worldwide.<sup>1</sup> A clear manifestation of CHD is calcification of the coronary arteries. The amount of coronary artery calcifications (CAC), i.e. coronary calcium score, is a strong and independent predictor of cardiac events, e.g. myocardial infarction or heart failure.<sup>2,3</sup> In CT, CAC is defined as a high density area of  $\geq 130$  HU<sup>4</sup> in the artery. Using this definition CAC is commonly quantified into CAC volume, mass or Agatston score.<sup>4</sup> The Agatston score is used most because it directly indicates a patient's risk of CHD events.

In a clinical setting the amount of CAC is routinely quantified in non-contrast-enhanced cardiac CT exams with ECG-synchronization. However, other CT scans that show the heart, like chest CT, are increasingly used for quantification of CAC and determination of CVD risk. Such scans are made about ten times more often<sup>5</sup> than ECG-synchronized cardiac CT and moreover,

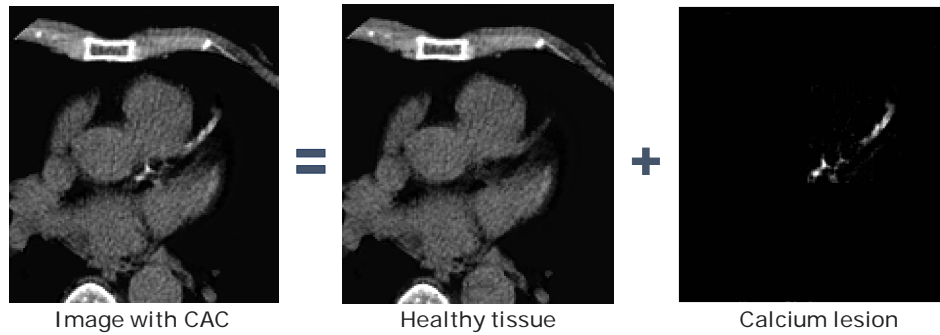


**Fig 1** An image containing coronary artery calcium (CAC) is decomposed into an healthy tissue image without CAC and an image containing only CAC.

the CAC scores in these scans correlate well with the CAC scores in cardiac CT.<sup>6,7</sup> Hence, given its clinical relevance, the guidelines of the Society of Cardiovascular Computed Tomography and the Society of Thoracic Radiology<sup>8</sup> recommend to quantify and report CAC on *all* non-contrast CTs showing the heart, including non-ECG-synchronized scans. However, the interscan reproducibility of calcium scores is limited. For example, the reported mean interscan variability of Agatston scores in cardiac CT with ECG-synchronization ranges from 15% to 41%.<sup>9-12</sup> Hence, in non-ECG-synchronized scans the limited interscan reproducibility is further emphasized due to increased influence of partial volume effect and cardiac motion. For instance, Jacobs et al.<sup>13</sup> reported an average interscan variability of 71% for Agatston scores in non-triggered chest CT scans, that led to assignment of different cardiovascular risk category in 24% of subjects. The compromised interscan reproducibility limits the applicability calcium quantification in non-ECG-synchronized scans in clinic and for longitudinal studies, in which reproducibility is of key importance to obtain reliable measurements.

The clinical definition that requires the use of the aforementioned single intensity level threshold at 130 HU has been identified as one of the major causes of the limited reproducibility of CAC quantification,<sup>14</sup> which may lead to under- or overestimation of the amount of CAC. This is especially pronounced in CT exams without ECG-synchronization where visualization of the calcifications is often extremely affected by cardiac motion. As a consequence, the calcifications are blurred or completely remain below the threshold. Nevertheless, common to the vast majority of manual and automatic calcium scoring methods is the use of the clinical definition that identifies voxels in the coronary arteries above the 130 HU threshold as CAC in an explicit manner (through segmentations)<sup>15,16</sup> or implicit manner (through regression of the CAC score).<sup>17,18</sup> To address this issue, automatic methods have been proposed that either use automatic adaptive thresholds or omit thresholding for segmentation of calcified lesions. Groen et al.<sup>19</sup> proposed using an adaptive threshold dependent on the maximum intensity value of each CAC lesion. Song et al.<sup>20</sup> proposed to adapt the threshold based on the intensity of the background in the vicinity of lesions in combi-

nation with deconvolution of the image, using a scanner-specific point spread function to decrease partial volume effect. Saur et al.<sup>21</sup> omitted the intensity threshold for segmentation by employing a mesh-based algorithm that segmented CAC lesions by refining their boundary based on the intensity value profile. A different method that circumvents thresholding for segmentation, was proposed by Šprem et al.,<sup>22</sup> who built on work by Dehmeshki et al.<sup>23</sup> Both used an expectation-maximization algorithm to determine the partial calcium content in each voxel of a CAC lesion and its vicinity.

While the aforementioned methods all show improved interscan reproducibility of CAC quantification, they use the clinically used CAC definition for initial lesion detection, thereby missing lesions below the intensity level threshold. This is particularly a problem with small lesions and scans with motion artefacts, where complete lesions may remain under the detection threshold. Although motion detection<sup>24</sup> in CAC lesions has been proposed, this does not include correction that would allow quantification of such CAC lesions.

To address the limited interscan reproducibility of CAC detection and quantification, we propose a method that does not depend on the current clinically used definition of CAC that requires intensity-level thresholding. Instead, we define CAC as the difference between an image visibly containing CAC and a healthy tissue image. Our method takes an image with CAC and decomposes it into an image without CAC and a CAC-map, i.e. an image showing only CAC (Figure 1). The CAC-map comprises the location of lesions and the grey values that indicate the attenuation in the CT scan due to CAC lesions. Due to this new definition of CAC lesions, our method can detect lesions that are completely - and partly - below the clinically used threshold.

Several earlier studies proposed to use an autoencoder for generating healthy counterparts of images with pathology in an unsupervised manner.<sup>25-27</sup> Subsequently, the pixel-wise intensity difference between the original image and the reconstruction was used to e.g. detect brain lesions in MRI scans,<sup>25</sup> brain CT,<sup>27</sup> or detected anomalies in head CT.<sup>26</sup> Alternative approaches used generative adversarial networks (GAN) for translating an image containing pathologies to a healthy image. Baur et al.<sup>28</sup> and Seah et al.<sup>29</sup> used conditional GANs to generate healthy images and used the difference with the input image for multiple sclerosis lesion segmentation, and visualizing features of congenital heart failure in chest X-rays, respectively. Furthermore, Baumgartner et al.<sup>30</sup> proposed to use a Wasserstein GAN to directly generate a difference map that indicates changes in the brain related to Alzheimer's disease. The map is added to the input image to create a healthy brain image from an image containing Alzheimer's disease. Tang et al.<sup>31</sup> proposed to predict both an healthy image and a difference map that indicates disease using a disentangled conditional GAN. To tackle the instability and mode collapse problems that often arise during training of GANs, Zhu et al.<sup>32</sup> proposed to use a cycle-consistency loss in their CycleGAN for image-to-image translation using natural images. Sun et al.<sup>33</sup> proposed to use a CycleGAN implementation for translating images containing lesions to healthy images. Subsequently, the pixel-wise intensity

difference was used to detect brain lesions in MRI and liver tumors in CT scans.

To decompose an image with CAC into an image without CAC and CAC-map, we employ a CycleGAN to translate images between the *containing CAC* domain and *not containing CAC* domain. To our knowledge, our method is the first to use a generative model for accurate segmentation of CAC lesions. The method builds on our preliminary work,<sup>34</sup> in which we presented a semi-automatic method for segmentation of CAC, that analyzed the vicinity of manually identified CAC lesions. The method was trained using clinical calcium scores as reference and hence, was not able to detect lesions below the threshold. In the current work, we extend the method to perform fully automatic CAC detection and quantification, including CAC lesions below the standard detection threshold. The method is aimed at scans where the low interscan reproducibility is most dire and therefore, experiments were performed in non-ECG-synchronized scans, with and without breathing motion, that often contain excessive cardiac motion artefacts and have a low spatial resolution. To simplify the challenging task and allow the method to focus on the region of interest only, CAC quantification was performed in the heart slices containing CAC. The method is developed and evaluated using 4,038 CT scans of 2,276 breast cancer patients and 626 CT scans of lung screening participants. Moreover, we show that the here proposed method outperforms the gold standard for calcium scoring in the clinic and a state-of-the-art automatic calcium scoring method in terms of interscan reproducibility of CAC quantification and detection of visible lesions.

## 2 Data

We confirm that all methods were carried out in accordance with relevant guidelines and regulations. We included 4,038 radiotherapy treatment planning (RTP) CTs of 2,276 breast cancer patients.<sup>35</sup> In this set 1,762 patients had two scans made on the same day: one with and one without breath-hold (Figure 2, A and B). Therefore, this set allows evaluation of CAC scoring interscan reproducibility. The remaining 514 patients had one CT scan made without breath-hold. Scans were acquired in the University Medical Center Utrecht with a Philips Brilliance Big Bore scanner. Intravenous (IV) contrast was not induced and the acquisition was not ECG-synchronized. The CTs were acquired with 120 kVp and reconstructed to 0.92-1.37 mm in-plane resolution and 3.0 mm slice thickness and increment. This study was approved and the need for informed consent was waived by the institutional review board of the University Medical Center Utrecht, the Netherlands.

Additionally, we included 626 low-dose chest CT images of 626 subjects included in the National Lung Screening Trail (NLST, Figure 2C). Scans were acquired in 29 different hospitals, on scanners from all major vendors.<sup>15,36</sup> Tube voltage was either set to 120 or 140 kVp, depending on the subjects weight. IV contrast was not induced and acquisition was not ECG-synchronized. Images were reconstructed to 0.49-0.98 mm in-plane resolution and 1.0-2.5 mm slice thickness and 0.6-2.5 mm increment.

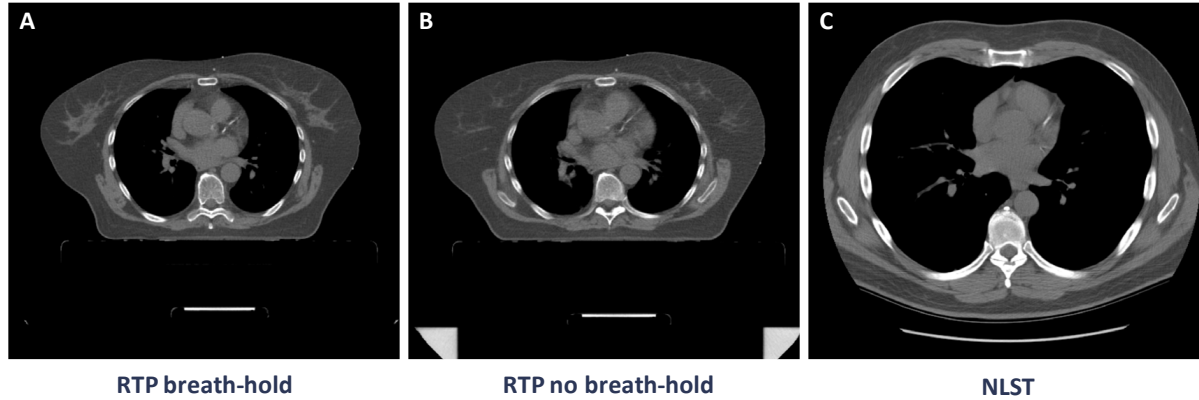


**Fig 2** Examples of two RTP scans of one breast cancer patient, one with breath-hold (A) and one without breath-hold (B), and an NLST scan of one participant (C).

Table 1 lists the used data sets, availability of reference annotations and describes the purpose of each data set. For development and training of the method, RTP CT scans of 514 patients with a single CT ( $RTP_{train}$  and  $RTP_{trainHS}$ ) and all 626 NLST scans ( $NLST_{train}$ ) were used. The latter were used to enhance training with a diverse set of scans of heavy smokers with high CAC burden. In method development, a validation set of 100 patients with two available RTP scans (200 scans) was used ( $RTP_{val}$ ). We divided the test scans into two sets with patient scan pairs:  $RTP_{test1}$ , a set consisting of scans of 119 patients totalling 238 RTP CTs with manually segmented CAC allowing detailed evaluation of calcium scoring; and  $RTP_{test2}$ , a set consisting of scans of 1,543 patients of in total 3,086 RTP CTs without reference CAC scores, used for assessment of interscan reproducibility.

To allow training, all training CTs, validation CTs and CTs from  $RTP_{test1}$  were manually labelled without using a threshold by an observer with  $>3$  years experience in calcium scoring. Because voxelswise annotation without a threshold is practically infeasible, as the exact outline of the CAC is not known, weak labels were used to train the methods. Therefore, the observer labelled axial slices of the scans as *containing CAC* or *not containing CAC*, based on visual assessment (Figure 3A). Moreover, for a subset of 199 RTP scans of the training set ( $RTP_{trainHS}$  and  $RTP_{testHS}$ ), manual segmentations of the heart were available from clinical practice.

To define reference standard for CAC, lesions were annotated and assigned coronary artery label in  $RTP_{test1}$ . Because accurate voxel-level manual annotation without threshold is hardly feasible, regions containing lesions were indicated in the scans, by rough manual voxel-painting without a threshold, with a brush size of 1 cm (Figure 3B). This was only done in the 34 scan pairs in which both scans had CAC, because pairs without CAC and visibly discordant pairs are not informative for measuring interscan reproducibility. Visibly discordant pairs are pairs in which in one scan CAC is visible and in the second scan it is not. Next, to allow comparison with calcium scoring used in clinic, manual annotations following the clinical definition from a previous study

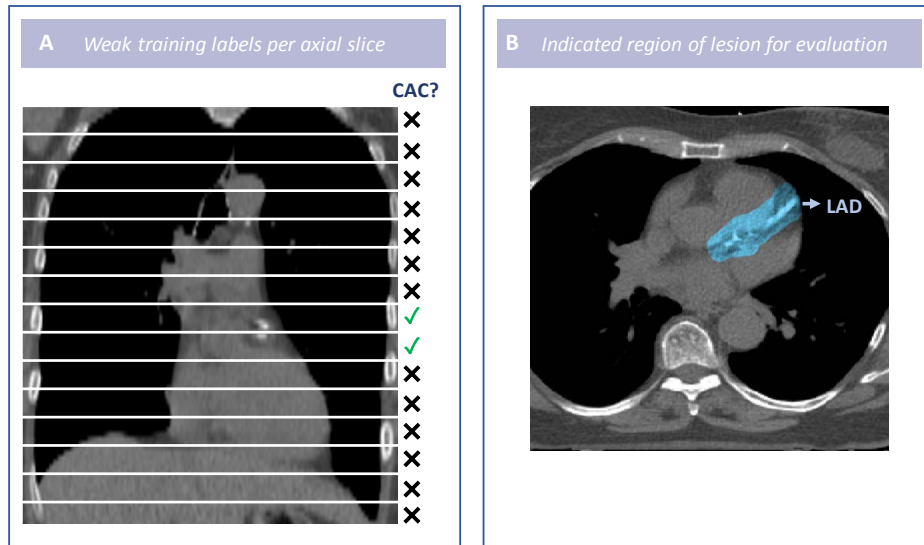


**Fig 3** Schematic example of the weak training labels per axial slice indicating whether CAC is present in the slice (A). Indicated region of the lesion with assigned coronary artery label (B).

for  $RT P_{test1}$  were available.<sup>16</sup>

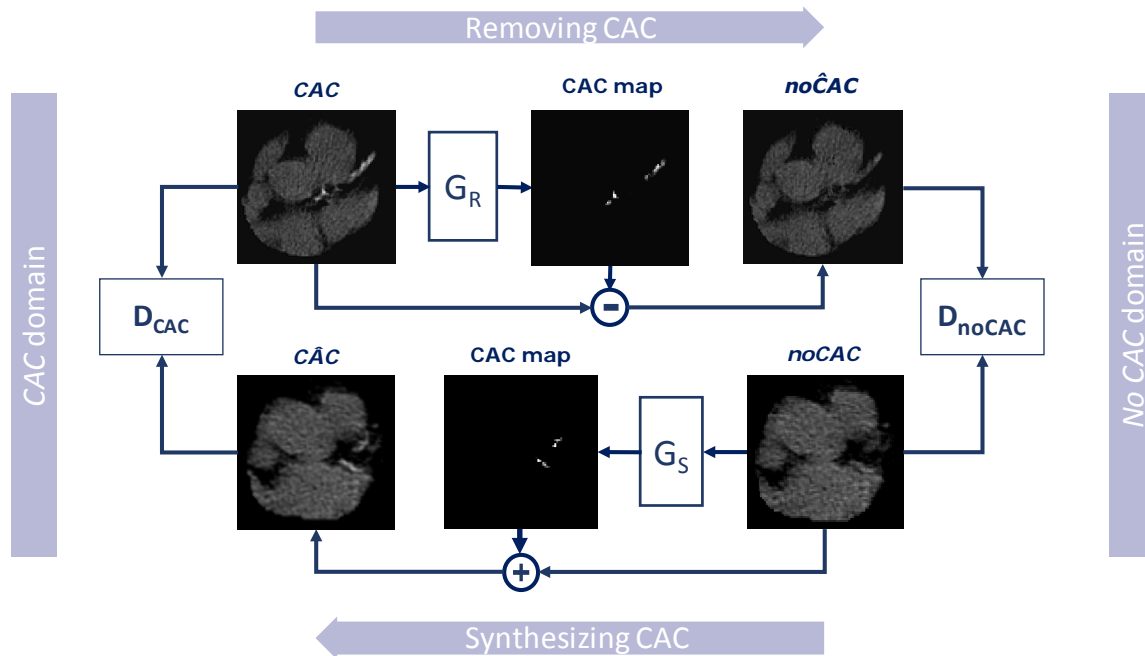


**Fig 4** Schematic overview of the proposed CycleGAN that translates the images from the domain of images with CAC (CAC domain) to the domain of images without CAC (No CAC domain) and back. In the pathway that removes CAC, a CAC map is predicted by the generator ( $G_R$ ) and subtracted from the image to obtain a synthetic image without CAC. In the pathway that synthesizes CAC the CAC map predicted by the generator ( $G_S$ ) is added to the image. Synthetic images are compared to real examples by discriminators (D).

**Table 1** A. Data sets, consisting of low-dose CT scans from the National Lung Screening Trial (NLST) or radiotherapy treatment planning (RTP) CT scans, used for development ( $NLST_{train}$ ,  $RTP_{train}$ ,  $RTP_{trainHS}$ ,  $RTP_{val}$ ) and evaluation ( $RTP_{testHS}$ ,  $RTP_{test1}$ ,  $RTP_{testlesions}$ ,  $RTP_{test2}$ ) of the presented method. Scans are made with (BH) or without deep inspiration breath-hold (nonBH). B. Availability of manual reference annotations are indicated per set for heart segmentations (Heart Segm.), labels per axial slice indicating presence of CAC as a binary decision assessed visually (Figure 3A) and availability of coarse segmentations of lesion regions (Lesion Regions, Figure 3B). C. The way the data is used in the experiments is listed as training (Tr), validation (Val) and testing (Test) for the different networks (Heart Segmentation, CAC Classification, Calcium CycleGAN).

<b>A</b>											
<b>Scan information</b>											
Scan Type		Patients	BH	nonBH							
<b>Development</b>											
$NLST_{train}$		626	626								
$RTP_{train}$		514		514							
$RTP_{trainHS}$		120		120							
$RTP_{val}$		100	100	100							
<b>Evaluation</b>											
$RTP_{testHS}$		79		79							
$RTP_{test1}$		119	119	119							
$RTP_{testlesions}$		34	34	34							
$RTP_{test2}$		1,543	1,543	1,543							
<b>B</b>											
<b>Reference Annotations</b>											
		Heart Segmentation	Per Slice CAC	Lesion Regions							
<b>Development</b>											
$NLST_{train}$			✓								
$RTP_{train}$			✓								
$RTP_{trainHS}$		✓									
$RTP_{val}$			✓								
<b>Evaluation</b>											
$RTP_{testHS}$		✓									
$RTP_{test1}$			✓								
$RTP_{testlesions}$			✓	✓							
$RTP_{test2}$											
<b>C</b>											
<b>Purpose</b>											
			Heart Segmentation			CAC Classification			Calcium CycleGAN		
			Tr	Val	Test	Tr	Val	Test	Tr	Val	Test
<b>Development</b>											
$NLST_{train}$						✓			✓		
$RTP_{train}$						✓			✓		
$RTP_{trainHS}$			✓	✓							
$RTP_{val}$						✓				✓	
<b>Evaluation</b>											
$RTP_{testHS}$					✓						
$RTP_{test1}$								✓			✓
$RTP_{testlesions}$								✓			✓
$RTP_{test2}$								✓			✓



**Table 2** Architecture of the Heart Segmentation CNN, CAC Classification CNN and the Generators in the proposed CycleGAN

	Heart Segmentation CNN	CAC Classification CNN	CAC-map generators CycleGAN
<b>General</b>			
Dimensions	3D	2D	2D
Input size	64x64x64 voxels	224x224 voxels	224x224 voxels
Type of padding (layers)	Zero (All)	Reflection (All)	Reflection (All)
<b>Architecture (kernel, output channels, stride)</b>			
1st Layer	Conv (7x7x7, 16)	Conv (7x7, 64)	Conv (7x7, 64)
2nd Layer	Conv (3x3x3, 32, 2)	Conv (3x3, 128, 2)	Conv (3x3, 128, 2)
3rd Layer	Conv (3x3x3, 64, 2)	Conv (3x3, 256, 2)	Conv (3x3, 256, 2)
ResNet Blocks	9 Blocks (3x3x3, 64, 1)	6 Blocks (3x3, 256, 1)	6 Blocks (3x3, 256, 1)
3rd last Layer	TConv (3x3x3, 32, 2)	-	TConv (3x3, 128, 2)
2nd last Layer	TConv (3x3x3, 16, 2)	Global Average Pool	TConv (3x3, 64, 2)
Last Layer	Conv (7x7x7, 2)	Dense Layer (256x2 channels)	Conv (7x7x7, 1)
Activation last Layer	Sigmoid	Softmax	Sigmoid

Conv = Convolution layer; TConv = Transposed convolution layer; All convolution layers, except the last layer, are followed by a batch normalization layer and rectifier linear unit activation. Resnet Blocks consist of 2 convolution layer pairs with a residual connection.

### 3 Method

We propose an automatic method that detects and segments CAC by decomposing a CT slice into an image without CAC and an image showing a CAC map, i.e. only CAC. By defining CAC as the difference between an image visibly containing CAC and a healthy tissue image, the method allows segmentation of whole lesions, including parts below the current clinical definition applying 130 HU threshold, leading to increased interscan reproducibility of CAC quantification.

The need for improved interscan reproducibility of CAC quantification is highest in non-ECG-synchronized scans. However, non-ECG-synchronized scans are typically made for other purposes than calcium scoring, thus, the field of view in these scans is highly variable. Therefore, before generating the CAC-map, we define the region of interest to simplify the CAC detection task by initial heart segmentation, and subsequent identification of CT slices with CAC.

Heart segmentation is performed with a 3D convolutional neural network (CNN), which, for efficiency, analyses the full image in a patch based manner. The network architecture is based on ResNet<sup>37</sup> and is detailed in Table 2, left. The Dice loss is used during training and Adam optimization algorithm ( $lr = 0.001$ ) is used for optimization. During inference, overlapping patches were analysed and the results were averaged for final prediction.

We classify each slice in the heart mask according to the presence of visible CAC with a 2D CNN with ResNet<sup>37</sup> based architecture (Table 2, middle). The CNN analyses axial image slices centered and cropped around the heart. For cropping, the center of mass of the heart segmentation is used. The network is trained with per slice labels indicating the presence of CAC, using the cross-entropy loss and Adam optimization algorithm ( $lr = 0.001$ ).



For the identified slices, we generate a CAC-map. Manually identifying voxels with visible CAC to directly predicts a CAC-map with a CNN, would be hardly feasible. Hence, we propose to obtain a CAC-map using weakly supervised labels, i.e. labels indicating whether CAC is present in the image. In our approach a CAC-map is obtained by subtracting a generated healthy tissue image from an image containing CAC. Because it is not possible to obtain paired CT scans of the same patient, where one would contain CAC and the other not, a paired approach for image generation is not feasible. Therefore, an unpaired approach is used to generate synthetic  $no\hat{C}AC$  images from images containing CAC. For this, images are assigned to two domains based on weak labels: one domain consisting of images containing visible CAC and the other domain containing images without visible CAC. Hence, to generate a healthy tissue image for subtraction, a 2D CycleGAN<sup>32</sup> for unpaired image-to-image translation is used to translate images from one domain to another. The CycleGAN is a type of GAN<sup>38</sup> that improves in training stability and performance over the traditional and conditional GAN, by adding cycle-consistency.<sup>32</sup>

The CycleGAN consists of two generators  $G$ , and two discriminators  $D$  that compete with each other. The generators are CNNs that convert an input image from either domain to a realistic image from the other domain. In our task the images are divided into the  $CAC$  domain that contains images with CAC and the  $noCAC$  domain that contains images without CAC. The discriminator CNNs compare the synthesized images against *real* examples from the target domain. In contrast to a conventional CycleGAN, that directly translates an input image to an image of the target domain, we use an adjusted CycleGAN (Figure 4) that adds an extra step to minimize data hallucination: in the removing pathway, images with CAC are translated to the  $noCAC$  domain by predicting a CAC map and subtracting it from the input image:  $no\hat{C}AC = CAC - G_R(CAC)$ . Hence, the CAC map  $G_R(CAC)$  comprises both the location of CAC lesions and grey values that indicate the attenuation in the CT scan due to CAC lesions. In the synthesizing pathway the CAC map  $G_S(noCAC)$  is added to the input image to generate a synthetic image containing CAC from an image without CAC:  $C\hat{A}C = noCAC + G_S(noCAC)$ . In this pathway the generator learns to synthesize realistic lesions based on probable lesion locations and severity inferred from the training data. In this work the synthesizing pathway is solely utilized for training stability. The generator in the pathway that removes CAC, i.e.  $G_R$ , is used to obtain the CAC map and, subsequently, the CAC map can be used to quantify the amount of CAC in the image.

The generators used in the CycleGAN for generating the CAC map have a ResNet-based architecture,<sup>37</sup> with 6 ResNet blocks using ReLU activation and no downsampling in between blocks (Table 2, right). To ensure the CAC maps only contain positive values, the generators have a sigmoid activation in the last layer. For the discriminator networks we use PatchGANs, which classify 70x70 overlapping image patches as real or synthetic, described in detail by.<sup>39</sup> The PatchGANs are able to capture high-frequency structure and have fewer parameters than a full-image discriminator and are therefore, easier to train.<sup>39</sup> The patch-level discriminators are applied to the image

in a fully convolutional manner, averaging all responses to provide the output of the discriminator.

The system is trained with the loss terms on the input and synthetic images that are traditionally used for training a CycleGAN:<sup>32</sup> Adversarial loss (Equation 2), Cycle-consistency loss (Equation 3) and Identity loss (Equation 4). The Identity loss trains  $G_R$  to predict an empty CAC-map when it is presented with an image without CAC and vice versa for  $G_S$ . Additionally, a Sparsity (L1) loss (Equation 5) on the CAC map is used to encourage the generator to predict sparse CAC maps, giving the full objective:

$$\mathbf{L} = \mathbf{L}_{Adversarial} + \lambda \mathbf{L}_{Cycle} + \alpha \mathbf{L}_{Identity} + \beta \mathbf{L}_{Sparsity} \quad (1)$$

Where

$$\begin{aligned} \mathbf{L}_{Adversarial} = & \mathbb{E}_{CAC \sim P_{data}(CAC)} [\log \mathbf{D}_{CAC}(CAC)] + \mathbb{E}_{noCAC \sim P_{data}(noCAC)} [\log(1 - \mathbf{D}_{CAC}(C\hat{A}C))] \\ & + \mathbb{E}_{noCAC \sim P_{data}(noCAC)} [\log \mathbf{D}_{noCAC}(noCAC)] \\ & + \mathbb{E}_{CAC \sim P_{data}(CAC)} [\log(1 - \mathbf{D}_{noCAC}(no\hat{C}AC))] \quad (2) \end{aligned}$$

$$\begin{aligned} \mathbf{L}_{Cycle} = & \mathbb{E}_{CAC \sim P_{data}(CAC)} \|\mathbf{G}_S(\mathbf{G}_R(CAC)) - CAC\|_1 \\ & + \mathbb{E}_{noCAC \sim P_{data}(noCAC)} \|\mathbf{G}_R(\mathbf{G}_S(noCAC)) - noCAC\|_1 \quad (3) \end{aligned}$$

$$\mathbf{L}_{Identity} = \mathbb{E}_{noCAC \sim P_{data}(noCAC)} \|\mathbf{G}_R(noCAC)\|_1 + \mathbb{E}_{CAC \sim P_{data}(CAC)} \|\mathbf{G}_S(CAC)\|_1 \quad (4)$$

$$\mathbf{L}_{Sparsity} = \mathbb{E}_{CAC \sim P_{data}(CAC)} \|\mathbf{G}_R(CAC)\|_1 + \mathbb{E}_{noCAC \sim P_{data}(noCAC)} \|\mathbf{G}_S(noCAC)\|_1 \quad (5)$$

To make the method more robust to noise, during training images are augmented by reducing or amplifying noise. To reduce the noise, images are smoothed with a Gaussian filter with  $\sigma = 0.5$  pixels. To amplify noise, a noise image is obtained by subtracting the smoothed image from the original input image that is, subsequently, added to the input image. Moreover, during training random cropping and rotation are used for augmentation.

Despite the sparsity loss, the generated CAC-map may contain low levels of noise, because of excessive image noise. Noise in the CAC map may lead to unrealistically low values for soft tissue in the synthetic noCAC image. Therefore, we mask voxels in the CAC-map that lead to a value of  $< -10$  HU in the synthetic noCAC image, as those are likely noise voxels in the CAC-map.

Finally, CAC was quantified by CAC pseudo-mass and adjusted Agatston score. The pseudo-mass was calculated by multiplying the sum of HU values of the voxels in the lesions by the voxel volume. The adjusted Agatston score was calculated by multiplying the area of a lesion with a density score (1:  $<199$  HU, 2: 200–299 HU, 3: 300–399 HU, 4:  $>399$  HU) determined by the maximum density of the area, and summing over axial slices. Please note that the adjusted Agatston score includes segmented (parts of) lesions below the clinically used threshold. For comparison, the conventional Agatston score was calculated based on segmentations obtained using the clinical definition, which uses the following density scores: 0:  $<130$  HU, 1: 130–199 HU, 2: 200–299 HU, 3: 300–399 HU, 4:  $>399$  HU. Please note that the adjusted Agatston score is equal

to the conventional Agatston score when CAC lesions are segmented using the 130 HU threshold according to the clinical definition of CAC.

## 4 Evaluation

Detection of CAC lesions was evaluated using accuracy, sensitivity, rate of false positive scans and F1-score, between the automatic and reference labels that indicated visible CAC.

The reproducibility of the CAC score was evaluated in scan pairs, using absolute relative differences of quantified CAC pseudo masses. To measure the interscan agreement of adjusted Agatston scores, the two-way random intraclass correlation coefficient (ICC) for absolute agreement was computed and Bland Altman plots with 95% limits of agreement were examined.<sup>40</sup> Moreover, patients were assigned one of four CHD risk categories (I: 0–10, II: 11–100, III: 101–400, IV: <400) based on their adjusted Agatston score. Agreement between risk categories of each patient determined from the patient’s two scans was evaluated using Cohen’s linearly weighted kappa ( $\kappa$ ).

## 5 Experiments and Results

We evaluate the detection performance of visible CAC and the interscan reproducibility of the proposed method. Moreover, we compare the performance of our method with two clinical calcium scoring methods that use the standard clinically used CAC definition for segmentation: manual calcium scoring and automatic calcium scoring with a validated, state-of-the-art deep learning approach.<sup>16</sup> Finally, we perform an ablation study to evaluate the different components of the method.

Prior to heart segmentation all scans were resampled to 1.5 mm in-plane resolution for standardization across the data set and 3.0 mm slice spacing, the slice spacing of manual reference annotations. The heart segmentation CNN was trained using  $RTP_{trainHS}$ : a subset of 120 radiotherapy treatment planning CT scans of  $RTP_{train}$ , for which reference heart segmentations were available. Of this set, 100 scans were used for training and 20 scans for validation.  $RTP_{testHS}$  was used for evaluation (see Table 1). The CNN was trained for 250,000 iterations with batches of 10 patches of 64x64x64 voxels. Batches were balanced for presence of the heart during training. After training, the heart segmentation CNN achieved a median Dice score of 0.95 (interquartile range 0.94-0.96), a median Hausdorff distance of 15 mm (interquartile range 11 - 21 mm) and a median asymmetric surface distance of 1.6 mm (interquartile range 1.2 - 2.2 mm) over all test images in  $RTP_{testHS}$ .

After the heart segmentation, images were resampled to 1.0 mm in-plane resolution, which was the average resolution of the training set, and 1.5 mm slice spacing, for comparison with clinical calcium scoring.<sup>16</sup> Moreover, slices were clipped between -50 HU and 950 HU, for optimal contrast between soft tissue and CAC, and scaled between 0 and 1. The training set of 626 low dose chest CTs ( $NLSST_{train}$ ) and 315 radiotherapy treatment planning CTs ( $RTP_{train}$ ) was used,

with in total 65,675 2D slices containing the heart. Given that the method is aimed for analysis of RTP CT, the validation set of 200 such scans of 100 breast cancer patients (100 pairs) was used ( $RTP_{val}$ , Table 1). During training manually defined reference labels indicating the presence of CAC in axial CT slices were used. The slice classification CNN was trained for 1,500,000 iterations using batches of 20 axial CT slices of 224x224 voxels. Batches were randomly sampled and balanced for presence of visible CAC. After training, the slice classification CNN achieved an per slice accuracy of 0.93, with a sensitivity of 0.78 for visible CAC and a false positive rate of 0.06, on all 17,450 CT slices from  $RTP_{test1}$  containing the heart. On average 9.9% of the slices containing the heart was analysed by the CycleGAN.

The adjusted CycleGAN for generating the CAC map was trained with the same data set and preprocessing as the slice classification CNN. The adjusted CycleGAN was trained for 375,000 iterations, after which the learning curves converged, using batches of 4 axial CT slices of 224x224 voxels, which was the maximum that fit in the available GPU memory. Batches were balanced for both the presence of CAC and relative slice position in the heart, using the heart segmentations. The training parameters were determined experimentally through qualitative (visual) and quantitative assessment. Qualitative assessment evaluated the appearance of the generated synthetic  $no\hat{C}AC$  and synthetic  $C\hat{A}C$  images, and it led to setting the learning rate to 0.0001 and  $\lambda$  to 10.<sup>32</sup> Thereafter, quantitative assessment was used to define parameters  $\alpha$  and  $\beta$  through evaluation of the CAC detection (F1-score) and CAC reproducibility (absolute relative difference) on  $RTP_{val}$ . Figure 5 shows the evaluated parameters and the obtained results. Based on these results,  $\alpha = 10$  and  $\beta = 0.001$  were used in further experiments. Finally, the predicted CAC maps were resampled to the original in-plane resolution prior to evaluation.

All experiments were performed using Python with Pytorch<sup>41</sup> on an Intel Xeon E5-1620 3.60 GHz CPU with an NVIDIA Titan X GPU. The complete analysis takes on average about 2 minutes per scan.

### 5.1 CAC detection per scan

In the clinic CAC is routinely detected on a scan-level and used for CVD risk prediction. To provide insight in the detection performance of visible CAC on a scan-level, Figure 7 illustrates the results and Figure 6A (proposed) shows the sensitivity, rate of false positive scans (FPR) and F1-score in  $RTP_{test1}$  (Table 1). The proposed method achieved a sensitivity for visible CAC of 0.83, with an FPR of 0.14, meaning 21 out of 150 scans without visible CAC, and an F1-score of 0.80. In comparison, the sensitivity was 0.69 and 0.67 for manual and automatic clinical calcium scoring, respectively. The F1-score of the clinical calcium scoring methods was comparable with our method, due to a low FPR. Among our false positive cases, in 10 cases a lesion in the aorta was erroneously detected (Figure 7, FP Aorta), among which 6 were located in the ostia of the coronary arteries. In 9 scans noise was detected as CAC by the proposed method. In 5 of these 9

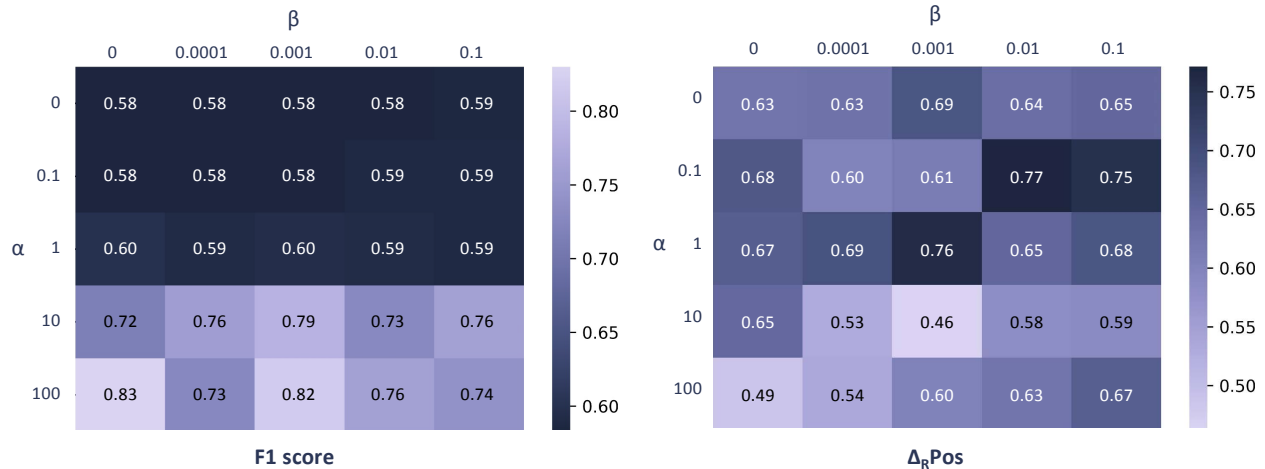


**Fig 5** F1 score for per scan CAC detection and per scan absolute relative difference for concordant positive scans on the validation set

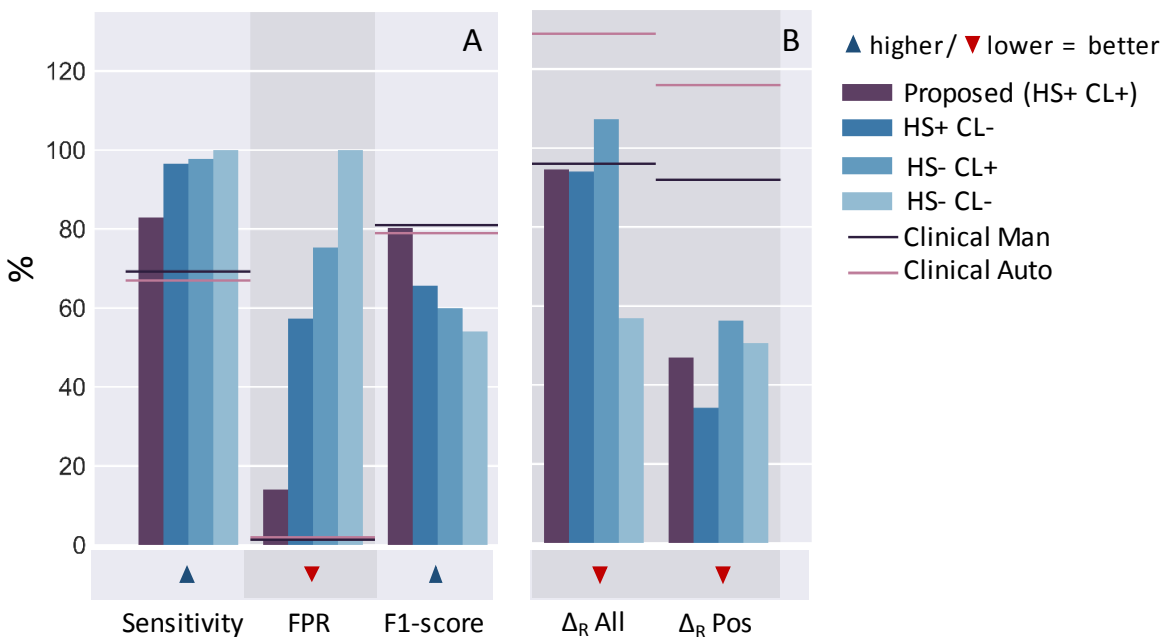


**Fig 6** The results of the ablation study for the method with and without heart segmentation (HS +/-) and with and without slice classification (CL +/-). We evaluated the detection performance (A) with sensitivity, false positive rate (FPR) and F1-score. We evaluated the interscan reproducibility (B) with absolute relative difference in CAC mass for all pairs ( $\Delta_R$  All) and concordant positive pairs ( $\Delta_R$  Pos). For comparison, the performance of clinical manual and clinical automatic calcium scoring are shown with horizontal lines.

scans, the false positive lesion was located near the edge of the heart segmentation (Figure 7, FP Noise).

As is shown in Figure 7, the proposed method also segments the parts of the calcium lesions that remain below the threshold. Particularly in lesions severely affected by motion, e.g. commonly

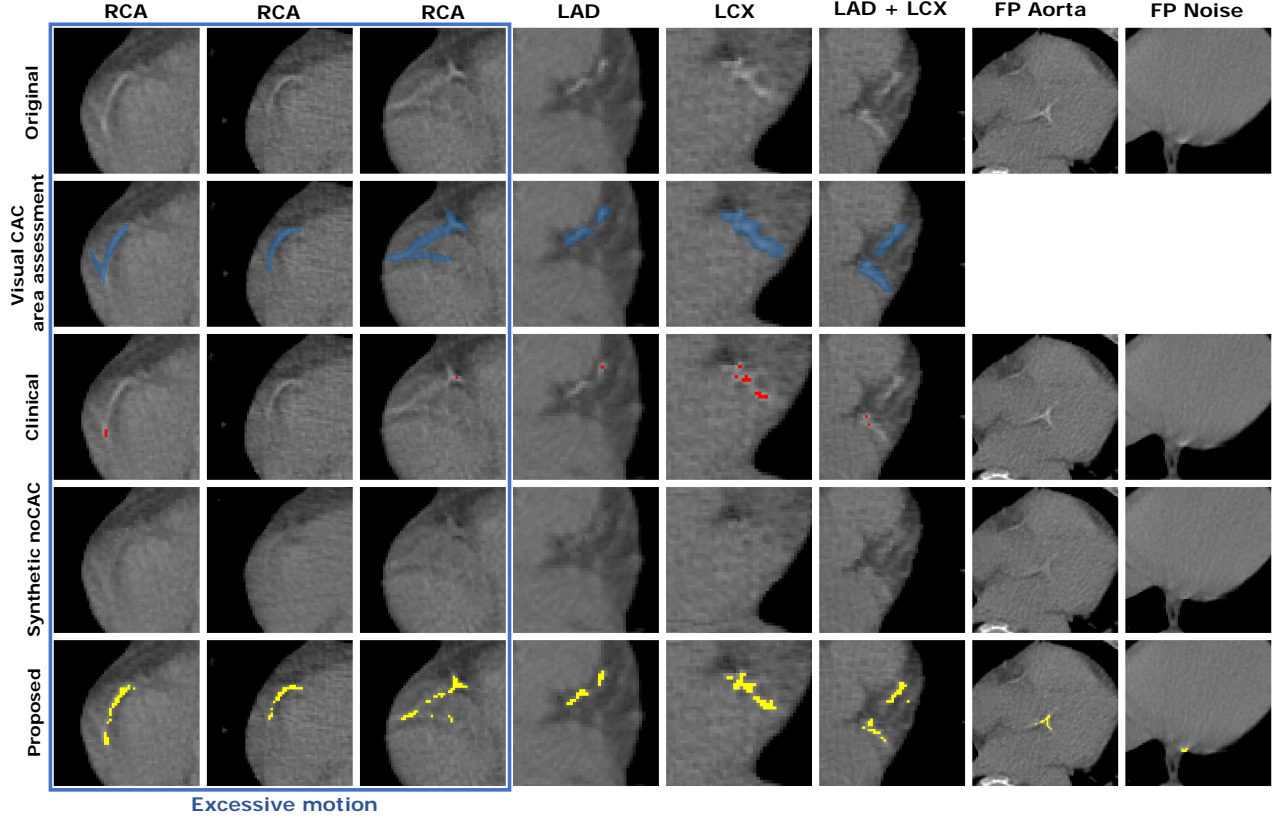


**Fig 7** Examples of lesions, visual assessment of the CAC lesion area, calcium segmentation using the clinical definition, corresponding synthetic images without CAC and segmentation of CAC with the proposed method and following the clinical protocol. Lesions with excessive motion are indicated with the blue box.

lesions in the RCA, the difference between the proposed method and manual clinical calcium scoring is especially pronounced.

### 5.2 CAC detection per artery

Because the impact of cardiac motion is different per location, we additionally evaluate the detection performance per artery. A subset of 34 concordant scan pairs from  $RT P_{test1}$  that contain CAC with per artery CAC annotations ( $RT P_{testlesions}$ ) were used for evaluation. Overall, the proposed method detected CAC in 81 out of 102 arteries with lesions (Table 3A, left). Out of 51 lesion pairs, the method detected both lesions in 34 pairs (Table 3A, right). In comparison, manual clinical calcium scoring detected 70 out of 102 single lesions, and automatic clinical calcium scoring detected 64 out of 102. Manual clinical calcium scoring detected CAC in both lesions in 30 out of 51 lesion pairs and automatic clinical calcium scoring detected 26 pairs out of 51. The achieved improvement of our method over the clinical methods was largest in the RCA, in which 64% of the visible lesions remained below the 130 HU threshold due to blurring caused by cardiac motion. This is also illustrated in Figure 7, where all lesions are affected by partial volume effect due to low resolution and especially lesions in the RCA are subject to excessive motion artefacts.



**Table 3** Per artery detection performance (A) and interscan reproducibility (B) of clinical manual ( $\text{Clinical}_M$ ) and automatic ( $\text{Clinical}_A$ ) calcium scoring, and the proposed method in  $RTP_{test1}$ . CAC detection is shown for pairs and for single scans. Reproducibility is evaluated with the absolute relative difference in CAC pseudo-mass in scan-rescan artery pairs for concordant positive artery pairs ( $\Delta_R\text{Pos}$ ) as well as all artery pairs ( $\Delta_R\text{All}$ ).

	(A)		(B)	
	Single (%)	Pairs (%)	$\Delta_R$ All	$\Delta_R$ Pos <sup>†</sup>
<b>Proposed</b>				
CAC	<b>81 (79)</b>	<b>34 (67)</b>	<b>0.95</b>	<b>0.55</b>
LAD	<b>57 (92)</b>	<b>26 (84)</b>	<b>0.84</b>	<b>0.61</b>
RCA	<b>16 (57)</b>	<b>5 (36)</b>	<b>1.25</b>	<b>0.35</b>
LCX	<b>8 (67)</b>	<b>3 (50)</b>	0.99	<b>0.33</b>
<b>Clinical<sub>M</sub></b>				
CAC	70 (69)	30 (59)	1.05	0.77
LAD	53 (85)	23 (74)	1.00	0.75
RCA	10 (36)	4 (29)	1.42	1.14
LCX	7 (58)	3 (50)	<b>0.84</b>	0.46
<b>Clinical<sub>A</sub></b>				
CAC	64 (63)	26 (51)	1.15	0.76
LAD	48 (77)	21 (68)	1.07	0.81
RCA	9 (32)	2 (14)	1.63	0.74
LCX	7 (58)	3 (50)	0.86	0.48

<sup>†</sup> Pairs in which CAC was detected in the artery in both scans by the respective method.

**Table 4** Reproducibility of CAC pseudo mass and Agatston scores for automatic clinical calcium scoring and the proposed method in  $RTP_{test2}$

	All pairs			Concordant positive pairs			
	CAC mass	AG score		n (%)	CAC mass	AG score	
1543 pairs	$\Delta_R$	ICC	ICC		$\Delta_R$	ICC	ICC
<b>Proposed</b>	0.88	0.97 (0.96-0.97)	0.96 (0.96-0.96)	515 (34%)	0.44	0.96 (0.96-0.97)	0.95(0.95-0.96)
<b>Clinical</b>	0.92	0.93 (0.92-0.94)	0.91 (0.91-0.92)	375 (24%)	0.58	0.92 (0.90-0.93)	0.90 (0.88-0.92)

### 5.3 Interscan reproducibility of CAC quantification

To make CAC quantification in non-ECG-synchronized CT scans useful for clinical application the interscan reproducibility ideally should be high. Therefore, the interscan reproducibility of CAC pseudo mass was evaluated in  $RTP_{test1}$ . First, we evaluated the absolute relative difference in CAC pseudo mass in 51 artery pairs using per artery annotations of lesions described in Section 2. The interscan difference was 95% on average in all artery pairs (Table 3B, left). In concordant positive artery pairs, i.e. pairs in which the method detected CAC in both arteries, the interscan difference was 55% using the proposed method (Table 3B, right). Second, we evaluated the reproducibility of total CAC pseudo mass in scan pairs. The interscan difference was 94% on average in all scan pairs (Figure 6B, left). For concordant positive scan pairs the absolute relative difference was 47% (Figure 6B, right). The higher absolute relative difference in CAC pseudo mass (i.e. lower reproducibility) in all scan pairs compared to positive pairs, is partly explained by the presence of 21 discordant pairs. In these pairs the method shows a high absolute relative difference, since



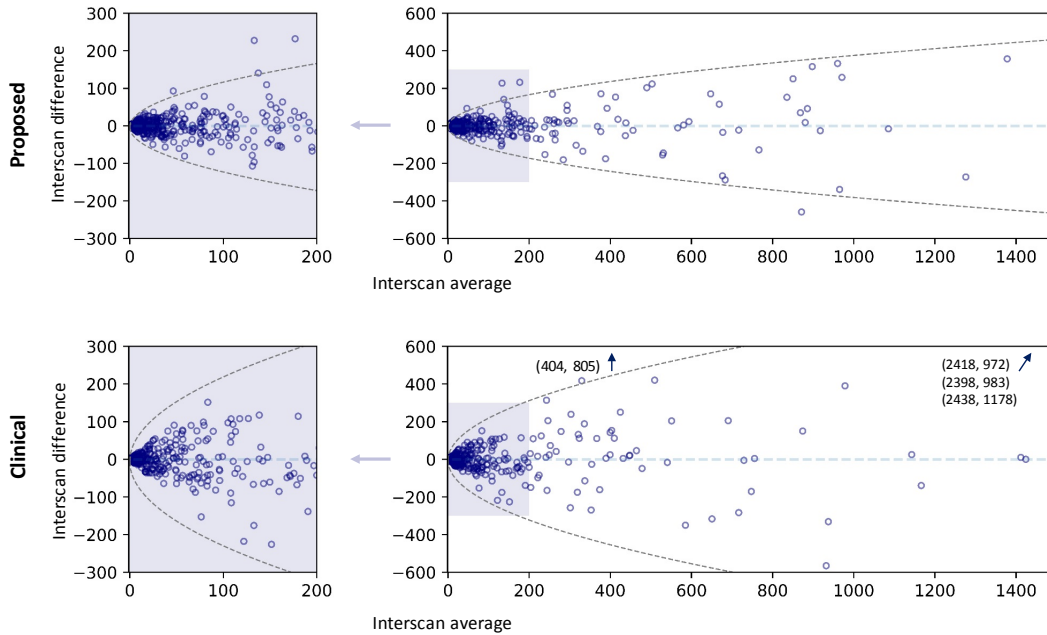


**Fig 8** Bland-Altman plots for adjusted Agatston scores of the proposed and automatic clinical method. For comparison purposes the adjusted Agatston scores of the proposed method are scaled to the range of scores of the clinical method. Please note that, since the same linear scaling is used for all scores, this does not influence the agreement. 95% limits of agreement are indicated by dashed lines. Because the errors tend to increase with increasing CAC, regression for nonuniform differences was used to model the variation of the absolute differences in scan pairs. To calculate the 95% limits of agreement, the predicted absolute differences were multiplied by  $1.96 \times (\pi/2)^{1/2}$ , because the absolute differences have a half-normal distribution.<sup>40</sup>

a CAC lesion is only visible in one of the two scans. Additionally, we compared our results to clinical calcium scoring. Both clinical methods show a lower interscan reproducibility than our proposed method in artery pairs as well as in scan pairs. For manual clinical calcium scoring the interscan difference was 77% in concordant positive artery pairs and 89% in concordant positive scan pairs. For automatic clinical calcium scoring the interscan difference was 76% and 114% in artery pairs and scan pairs, respectively. For similar reasons as for our method, the relative interscan difference is high when all scan pairs are considered.

Moreover, the reproducibility of the proposed method is evaluated in  $RTP_{test2}$ , in which manual annotations are not available. Hence, the results of our method are compared with automatic clinical calcium scoring. The results are listed in Table 4. The relative difference in CAC mass for positive pairs with detected CAC in both scans was 44%. For all scan pairs this was 88%. Moreover, the interscan agreement of CAC mass was high with an ICC of 0.96 (95% CI 0.96-0.97) in positive pairs and 0.97 (95% CI 0.96-0.97) in all pairs. In comparison, the relative difference was 58% in concordant positive pairs and 92% in all pairs when using the automatic clinical method.

**Table 5** Interscan agreement of risk categorization based on (adjusted) Agatston score in  $RTP_{test1}$  and  $RTP_{test2}$ . The risk categories are I: 0-10, II: 11-100, III: 101-400, IV:  $\geq 400$ .

	<b>Proposed<sup>†</sup></b>	<b>Clinical<sub>M</sub></b>	<b>Clinical<sub>A</sub></b>
<i>RTP<sub>test1</sub></i>			
$\kappa$	0.82 (0.71-0.94)	0.63 (0.42-0.84)	0.64 (0.41-0.87)
Accuracy	0.92	0.92	0.95
<i>RTP<sub>test2</sub></i>			
All pairs			
$\kappa$	0.84 (0.82-0.87)	-	0.81 (0.78-0.84)
Accuracy	0.90	-	0.92
Concordant positive pairs <sup>‡</sup>			
$\kappa$	0.77 (0.72-0.82)	-	0.67 (0.61-0.72)
Accuracy	0.79	-	0.68

<sup>†</sup> For comparison purposes, the adjusted Agatston scores obtained with the proposed method were linearly scaled to the range of the scores obtained with automatic clinical (Clinical<sub>A</sub>) calcium scoring, using the mean score of both methods.

<sup>‡</sup> Pairs in which the Clinical<sub>A</sub> method found CAC in both scans.

Moreover, the ICC for the quantified CAC mass was significantly lower for the clinical automatic method than for the proposed method (Table 4).

The proposed method achieved an interscan agreement for adjusted Agatston scores with an ICC of 0.96 (95% CI 0.96-0.96). This is significantly better than for the automatic clinical method that achieved an ICC of 0.91 (95% CI 0.91-0.92). This improvement is clearly visible in the Bland-Altman plots (Figure 8), where the 95% limits of agreement are narrower for the proposed method than for automatic clinical calcium scoring.

#### 5.4 Ablation Study

To investigate the benefits of prior heart segmentation and slice classification, we evaluated performance using the following settings: 1) using the settings as proposed, 2) the proposed method without slice classification, where all CT slices of the heart were analysed, 3) the proposed method without heart segmentation, 4) the proposed method without heart segmentation and without slice classification. When heart segmentation was not used, we standardized the field of view over the data sets to include the heart and chest wall. CAC detection, FPR and absolute relative interscan difference of the quantified CAC mass was evaluated on  $RTP_{test1}$ . Figure 6 shows the results. The proposed method achieved the best performance, with an F1-score of 0.80 and an absolute relative difference in CAC mass of 47%. While both approaches without slice classification show a high sensitivity, the false positive rate is high: with settings 2 the method found false positive lesions in all negative scans and with settings 4 in 57% of the negative scans. The effect of defining the region of interest by heart segmentation is not only reflected in a better detection, but also in a higher interscan reproducibility of CAC mass, i.e. lower absolute relative difference.

### 5.5 Risk category assignment

Because CVD risk stratification based on the Agatston score is clinically relevant, we evaluate the interscan reproducibility of risk categorization. The interscan agreement of CVD risk categories is shown in Table 5. The agreement in  $RTP_{test1}$  was higher using scores derived with the proposed ( $\kappa = 0.82$ ) method than with manual or automatic clinical calcium scoring, with  $\kappa$  of 0.63 and 0.64 respectively. In concordant positive pairs of  $RTP_{test2}$  the  $\kappa$  was 0.77 for the proposed method. In contrast, for automatic clinical calcium scoring this was 0.67.

## 6 Discussion

We presented a method for calcium scoring that does not depend on the standard clinically used definition of CAC that applies an intensity value threshold of 130 HU for segmentation of CAC lesions. Instead, our method defines CAC as the difference between an image visibly containing CAC and a healthy tissue image. Hence, the method can identify CAC - complete or parts of lesions - that may remain undetected by the clinical threshold due to e.g. partial volume effect in small lesions or blurring due to cardiac motion. We achieve this by separating an image containing CAC into an image without CAC and an image only containing CAC. For this we exploit a CycleGAN that translates images between the CAC and noCAC domain. We have shown that segmentation of lesions using our method enables increased interscan reproducibility of CAC quantification, compared to clinically used manual and automatic CAC scoring. Increased interscan reproducibility may lead to more reliable risk estimation and enable longitudinal studies in non-ECG-synchronized CT.

Previous research shows that interscan reproducibility in non-ECG synchronized CT scans is lower than in dedicated cardiac CT.<sup>9-12</sup> Because of limitations in the acquisition of radiotherapy treatment planning CTs, our method does not exceed the in literature reported reproducibility in dedicated cardiac CT. However, CAC scoring is increasingly performed in non-dedicated CT scans, hence, the need for more reproducible CAC quantification is growing, especially for quantification in challenging scans like the ones used in this work. Our proposed method shows potential for increasing the interscan reproducibility in non-ECG synchronized scans to the level of dedicated cardiac CT.

In contrast to clinical methods, the proposed method is able to detect visible CAC lesions that remain below the threshold. Owing to a more accurate segmentation that includes pairs of lesions below the threshold, our method outperforms clinical CAC scoring methods in interscan reproducibility of CAC quantification. The results of per artery evaluation show that this improvement was especially pronounced for CAC in the RCA. This is probably due to the ability of the proposed method to detect parts of lesions that are heavily affected by motion artefacts, which occurs more for the lesions in the RCA than in the LAD and LCX.

Errors were made in a number of scans. False positive detections mostly consisted of noise in the proximity of an artery or other types of calcifications than CAC, such as calcifications in the aorta or cardiac valves. Despite noise augmentation during training and post processing, the CAC map contained noise in a few cases. Such errors were often located close to the apex and near the RCA, where the noise level was most severe. Noise reduction strategies described in e.g. Wolterink et al.<sup>42</sup> could offer a solution. False positives in the aorta or valves were often close to the ostia of the coronaries or occurred in the mitral valve. Since in scans without ECG triggering it is often difficult to distinguish CAC from calcifications in the thoracic aorta or mitral valve calcifications, these type of errors are also not uncommon for human observers<sup>43</sup> and are also present in other automatic methods.<sup>15-17</sup> False negative lesions were typically small with very low voxel intensities, making them difficult to distinguish from noise and soft tissue, also for experts.

Similarly to our preliminary work,<sup>34</sup> the method without heart segmentation and slice classification suffered from a large amount of false positives in the CAC map, which made fully automatic quantification of CAC infeasible. In our ablation experiment, we showed that adding slice classification with respect to CAC presence and heart segmentation solves this issue. Using classification to identify the slices containing CAC, prevents false positive errors in slices that do not contain CAC. By adding heart segmentation, we prevent anatomical structures outside the heart in the data from influencing the CAC segmentation, resulting in more reproducible quantification. Likewise, in previous methods for CAC quantification in scans with high noise levels, a false positive reduction step was used to decrease the number of false positive findings.<sup>15,16</sup> Possibly, if a very large amount of training data would be available, the method would be able to learn to avoid these errors. However, in the medical field this is often challenging to obtain. In this work, heart segmentation and slice classification are performed independently. Although they are relatively straightforward, future work will investigate merging these steps into a single network.

The heart segmentation network showed good performance in terms of Dice and asymmetric surface distance. However, a relatively high Hausdorff distance was found. Visual evaluation revealed that errors causing high Hausdorff distance were mostly located in the basal slices of the heart. This is probably due to high interobserver variability in reference segmentations regarding the difficult to outline superior boundaries of the heart. Given that the segmented superior boundaries are typically well above the ostia of the coronaries, we expect the influence of variability in the superior boundaries of the heart on CAC classification and quantification to be minimal.

During experiments the impact of the different loss terms for training the Calcium CycleGAN on the CAC detection and reproducibility was evaluated using relatively large differences in the values of the tested parameters. Possibly a performance gain can be achieved by further optimizing  $\alpha$  and  $\beta$ . Nevertheless, given the obtained results (Figure 5), we expect the benefit would be limited.

Other approaches for increasing the reproducibility of CAC quantification have previously been

proposed.<sup>19-23</sup> Since the true amount of CAC is not available for patients, often a phantom is used for development and evaluation of the method. This makes direct comparison of our method infeasible. Šprem et al.<sup>22</sup> additionally evaluated their approach in a set of 293 subject CT scans and showed an improved reproducibility of CAC volume between different CT images. However, different reconstructions of the same acquisition were used, excluding interscan differences, in contrast to two separate acquisitions used in our study. Moreover, in contrast to our approach a major drawback of previously proposed methods is the use of the standard 130 HU intensity threshold for detection of CAC prior to partial volume correction, inevitably missing lesions below the threshold.

Risk categorization of subjects is typically done using total CAC Agatston scores. However, the proposed method also includes parts of lesions below the clinical threshold, and thus, the Agatston score tends to be (substantially) higher than for the clinical methods. Therefore, assigning risk categories based on the Agatston score derived with the proposed method would necessarily lead to different definitions of CVD risk categories. In order to estimate the performance of risk categorization of the proposed method, the obtained Agatston scores were scaled to the range of clinical Agatston scores. The results showed an improved agreement for the proposed method, compared to automatic clinical calcium scoring. However, to establish the clinical relevance, further research relating the adjusted Agatston scores with CHD events is warranted.

Future research on evaluation of the proposed method in non-ECG-synchronized against calcium scoring in dedicated calcium scoring CT is needed. However, clinical calcium scoring in dedicated cardiac CT also suffers from low reproducibility.<sup>9-12</sup> A non-invasive imaging-based reference that indicates the true amount of CAC does not exist. Hence, to define the clinical relevance, future research investigating whether more reproducible CAC quantification with the proposed method leads to better prediction of CVD events is warranted. However, since CVD related outcomes were not available, investigating the relation to CVD events is out of scope of this work.

## **7 Conclusion**

We have proposed a method for detection and quantification of CAC in non ECG-synchronized chest CT scans that that does not require the application of the clinically used intensity level threshold. Hence, the method allows detection of visible CAC that may not exceed the standardly used 130 HU threshold due to e.g. partial volume effect or blurring due to cardiac motion. This leads to more reproducible quantification of CAC and increased interscan reproducibility of risk categorization compared to the current clinical method.

## **Disclosures**

The authors declare no competing interests.

## Acknowledgment

The authors gratefully acknowledge the Dutch Cancer Society for the financial support (NCT03206333). The authors thank the National Cancer Institute for access to NCI's data collected by the National Lung Screening Trial. The statements contained herein are solely those of the authors and do not represent or imply concurrence or endorsement by NCI.

## References

- 1 Wang, H., Naghavi, M., Allen, C., Barber, R. M., Bhutta, Z. A., Carter, A., Casey, D. C., Charlson, F. J., Chen, A. Z., Coates, M. M., et al., "Global, regional, and national life expectancy, all-cause mortality, and cause-specific mortality for 249 causes of death, 1980–2015: a systematic analysis for the global burden of disease study 2015," *The Lancet* **388**(10053), 1459–1544 (2016).
- 2 Hecht, H. S., "Coronary artery calcium scanning: past, present, and future," *JACC: Cardiovascular Imaging* **8**(5), 579–596 (2015).
- 3 Budoff, M. J., Nasir, K., McClelland, R. L., Detrano, R., Wong, N., Blumenthal, R. S., Kondos, G., and Kronmal, R. A., "Coronary calcium predicts events better with absolute calcium scores than age-sex-race/ethnicity percentiles: MESA (Multi-Ethnic Study of Atherosclerosis)," *Journal of the American College of Cardiology* **53**(4), 345–352 (2009).
- 4 Agatston, A. S., Janowitz, W. R., Hildner, F. J., Zusmer, N. R., Viamonte, M., and Detrano, R., "Quantification of coronary artery calcium using ultrafast computed tomography," *Journal of the American College of Cardiology* **15**(4), 827–832 (1990).
- 5 De González, A. B., Mahesh, M., Kim, K.-P., Bhargavan, M., Lewis, R., Mettler, F., and Land, C., "Projected cancer risks from computed tomographic scans performed in the united states in 2007," *Archives of internal medicine* **169**(22), 2071–2077 (2009).
- 6 Wu, M.-T., Yang, P., Huang, Y.-L., Chen, J.-S., Chuo, C.-C., Yeh, C., and Chang, R.-S., "Coronary arterial calcification on low-dose ungated mdct for lung cancer screening: concordance study with dedicated cardiac ct," *American Journal of Roentgenology* **190**(4), 923–928 (2008).
- 7 Budoff, M. J., Nasir, K., Kinney, G. L., Hokanson, J. E., Barr, R. G., Steiner, R., Nath, H., Lopez-Garcia, C., Black-Shinn, J., and Casaburi, R., "Coronary artery and thoracic calcium on noncontrast thoracic ct scans: comparison of ungated and gated examinations in patients from the copd gene cohort," *Journal of cardiovascular computed tomography* **5**(2), 113–118 (2011).
- 8 Hecht, H. S., Cronin, P., Blaha, M. J., Budoff, M. J., Kazerooni, E. A., Narula, J., Yankelevitz, D., and Abbara, S., "2016 SCCT/STR guidelines for coronary artery calcium scoring

- of noncontrast noncardiac chest CT scans: A report of the society of cardiovascular computed tomography and society of thoracic radiology,” *Journal of Cardiovascular Computed Tomography* **11**(1), 74–84 (2017).
- 9 Detrano, R. C., Anderson, M., Nelson, J., Wong, N. D., Carr, J. J., McNitt-Gray, M., and Bild, D. E., “Coronary calcium measurements: effect of CT scanner type and calcium measure on rescan reproducibility: MESA study,” *Radiology* **236**(2), 477–484 (2005).
  - 10 Mao, S., Bakhsheshi, H., Lu, B., Liu, S. C., Oudiz, R. J., and Budoff, M. J., “Effect of electrocardiogram triggering on reproducibility of coronary artery calcium scoring,” *Radiology* **220**(3), 707–711 (2001).
  - 11 Hoffmann, U., Siebert, U., Bull-Stewart, A., Achenbach, S., Ferencik, M., Moselewski, F., Brady, T. J., Massaro, J. M., and O’Donnell, C. J., “Evidence for lower variability of coronary artery calcium mineral mass measurements by multi-detector computed tomography in a community-based cohort—consequences for progression studies,” *European Journal of Radiology* **57**(3), 396–402 (2006).
  - 12 Van Hoe, L. R., De Meerleer, K. G., Leyman, P. P., and Vanhoenacker, P. K., “Coronary artery calcium scoring using ecg-gated multidetector CT: effect of individually optimized image-reconstruction windows on image quality and measurement reproducibility,” *American Journal of Roentgenology* **181**(4), 1093–1100 (2003).
  - 13 Jacobs, P. C., Işgum, I., Gondrie, M. J., Mali, W. P. T. M., van Ginneken, B., Prokop, M., and van der Graaf, Y., “Coronary artery calcification scoring in low-dose ungated CT screening for lung cancer: interscan agreement,” *American Journal of Roentgenology* **194**(5), 1244–1249 (2010).
  - 14 Hong, C., Bae, K. T., and Pilgram, T. K., “Coronary artery calcium: accuracy and reproducibility of measurements with multi-detector row CT—assessment of effects of different thresholds and quantification methods,” *Radiology* **227**(3), 795–801 (2003).
  - 15 Lessmann, N., van Ginneken, B., Zreik, M., de Jong, P. A., de Vos, B. D., Viergever, M. A., and Işgum, I., “Automatic calcium scoring in low-dose chest CT using deep neural networks with dilated convolutions,” *IEEE Transactions on Medical Imaging* **37**(2), 615–625 (2017).
  - 16 van Velzen, S. G., Lessmann, N., Velthuis, B. K., Bank, I. E., van den Bongard, D. H., Leiner, T., de Jong, P. A., Veldhuis, W. B., Correa, A., Terry, J. G., et al., “Deep learning for automatic calcium scoring in CT: validation using multiple cardiac CT and chest CT protocols,” *Radiology* **295**(1), 66–79 (2020).
  - 17 de Vos, B. D., Wolterink, J. M., Leiner, T., de Jong, P. A., Lessmann, N., and Işgum, I., “Direct automatic coronary calcium scoring in cardiac and chest CT,” *IEEE Transactions on Medical Imaging* (2019).



- 18 Cano-Espinosa, C., González, G., Washko, G. R., Cazorla, M., and Estépar, R. S. J., “Automated agatston score computation in non-ecg gated CT scans using deep learning,” in [*Medical Imaging 2018: Image Processing*], **10574**, 105742K, International Society for Optics and Photonics (2018).
- 19 Groen, J., Dijkstra, H., Greuter, M., and Oudkerk, M., “Threshold adjusted calcium scoring using CT is less susceptible to cardiac motion and more accurate,” *Medical Physics* **36**(2), 438–446 (2009).
- 20 Song, Y., Eck, B. L., Levi, J., and Wilson, D. L., “Improved reproducibility of calcium mass score using deconvolution and partial volume correction,” in [*Medical Imaging 2019: Biomedical Applications in Molecular, Structural, and Functional Imaging*], **10953**, 109531O, International Society for Optics and Photonics (2019).
- 21 Saur, S. C., Alkadhi, H., Desbiolles, L., Székely, G., and Cattin, P. C., “ACCURATUM: improved calcium volume scoring using a mesh-based algorithm—a phantom study,” *European Radiology* **19**(3), 591–598 (2009).
- 22 Šprem, J., De Vos, B. D., Lessmann, N., Van Hamersvelt, R. W., Greuter, M. J., De Jong, P. A., Leiner, T., Viergever, M. A., and Išgum, I., “Coronary calcium scoring with partial volume correction in anthropomorphic thorax phantom and screening chest CT images,” *PloS One* **13**(12), e0209318 (2018).
- 23 Dehmeshki, J., Ye, X., Amin, H., Abaei, M., Lin, X., and Qanadli, S. D., “Volumetric quantification of atherosclerotic plaque in CT considering partial volume effect,” *IEEE Transactions on Medical Imaging* **26**(3), 273–282 (2007).
- 24 Šprem, J., de Vos, B. D., Lessmann, N., de Jong, P. A., Viergever, M. A., and Išgum, I., “Impact of automatically detected motion artifacts on coronary calcium scoring in chest computed tomography,” *Journal of Medical Imaging* **5**(4), 044007 (2018).
- 25 Chen, X. and Konukoglu, E., “Unsupervised detection of lesions in brain mri using constrained adversarial auto-encoders,” in [*International Conference on Medical Imaging with Deep Learning*], (2018).
- 26 Sato, D., Hanaoka, S., Nomura, Y., Takenaga, T., Miki, S., Yoshikawa, T., Hayashi, N., and Abe, O., “A primitive study on unsupervised anomaly detection with an autoencoder in emergency head CT volumes,” in [*Medical Imaging 2018: Computer-Aided Diagnosis*], **10575**, 105751P, International Society for Optics and Photonics (2018).
- 27 Pawlowski, N., Lee, M. C., Rajchl, M., McDonagh, S., Ferrante, E., Kamnitsas, K., Cooke, S., Stevenson, S., Khetani, A., Newman, T., et al., “Unsupervised lesion detection in brain CT using bayesian convolutional autoencoders,” in [*International Conference on Medical Imaging with Deep Learning*], (2018).

- 28 Baur, C., Wiestler, B., Albarqouni, S., and Navab, N., “Deep autoencoding models for unsupervised anomaly segmentation in brain MR images,” in [*International MICCAI Brainlesion Workshop*], 161–169, Springer (2018).
- 29 Seah, J. C., Tang, J. S., Kitchen, A., Gaillard, F., and Dixon, A. F., “Chest radiographs in congestive heart failure: visualizing neural network learning,” *Radiology* **290**(2), 514–522 (2019).
- 30 Baumgartner, C. F., Koch, L. M., Can Tezcan, K., Xi Ang, J., and Konukoglu, E., “Visual feature attribution using wasserstein gans,” in [*Proceedings of the IEEE Conference on Computer Vision and Pattern Recognition*], 8309–8319 (2018).
- 31 Tang, Y., Tang, Y., Zhu, Y., Xiao, J., and Summers, R. M., “A disentangled generative model for disease decomposition in chest x-rays via normal image synthesis,” *Medical Image Analysis* **67**, 101839 (2021).
- 32 Zhu, J.-Y., Park, T., Isola, P., and Efros, A. A., “Unpaired image-to-image translation using cycle-consistent adversarial networks,” in [*Proceedings of the IEEE International Conference on Computer Vision*], 2223–2232 (2017).
- 33 Sun, L., Wang, J., Huang, Y., Ding, X., Greenspan, H., and Paisley, J., “An adversarial learning approach to medical image synthesis for lesion detection,” *IEEE Journal of Biomedical and Health Informatics* (2020).
- 34 van Velzen, S. G., de Vos, B. D., Verkooijen, H. M., Leiner, T., Viergever, M. A., and Išgum, I., “Coronary artery calcium scoring: Can we do better?,” in [*Medical Imaging 2020: Image Processing*], **11313**, 113130G, International Society for Optics and Photonics (2020).
- 35 Emaus, M. J., Išgum, I., van Velzen, S. G., van den Bongard, H. D., Gernaat, S. A., Lessmann, N., Sattler, M. G., Teske, A. J., Penninkhof, J., Meijer, H., et al., “Bragatston study protocol: a multicentre cohort study on automated quantification of cardiovascular calcifications on radiotherapy planning CT scans for cardiovascular risk prediction in patients with breast cancer,” *BMJ Open* **9**(7), e028752 (2019).
- 36 National Lung Screening Trial Research Team, “Reduced lung-cancer mortality with low-dose computed tomographic screening,” *New England Journal of Medicine* **365**(5), 395–409 (2011).
- 37 He, K., Zhang, X., Ren, S., and Sun, J., “Deep residual learning for image recognition,” in [*Proceedings of the IEEE Conference on Computer Vision and Pattern Recognition*], 770–778 (2016).
- 38 Goodfellow, I., Pouget-Abadie, J., Mirza, M., Xu, B., Warde-Farley, D., Ozair, S., Courville, A., and Bengio, Y., “Generative adversarial nets,” in [*Advances in Neural Information Processing Systems*], 2672–2680 (2014).

- 39 Isola, P., Zhu, J.-Y., Zhou, T., and Efros, A. A., “Image-to-image translation with conditional adversarial networks,” in [*Proceedings of the IEEE Conference on Computer Vision and Pattern Recognition*], 1125–1134 (2017).
- 40 Sevrukov, A. B., Bland, J. M., and Kondos, G. T., “Serial electron beam CT measurements of coronary artery calcium: has your patient’s calcium score actually changed?,” *American Journal of Roentgenology* **185**(6), 1546–1553 (2005).
- 41 Paszke, A., Gross, S., Massa, F., Lerer, A., Bradbury, J., Chanan, G., Killeen, T., Lin, Z., Gimelshein, N., Antiga, L., Desmaison, A., Kopf, A., Yang, E., DeVito, Z., Raison, M., Tejani, A., Chilamkurthy, S., Steiner, B., Fang, L., Bai, J., and Chintala, S., “Pytorch: An imperative style, high-performance deep learning library,” in [*Advances in Neural Information Processing Systems 32*], Wallach, H., Larochelle, H., Beygelzimer, A., d'Alché-Buc, F., Fox, E., and Garnett, R., eds., 8024–8035, Curran Associates, Inc. (2019).
- 42 Wolterink, J. M., Leiner, T., Viergever, M. A., and Išgum, I., “Generative adversarial networks for noise reduction in low-dose CT,” *IEEE Transactions on Medical Imaging* **36**(12), 2536–2545 (2017).
- 43 van Hamersvelt, R. W., Willemink, M. J., Takx, R. A., Eikendal, A. L., Budde, R. P., Leiner, T., Mol, C. P., Išgum, I., and de Jong, P. A., “Cardiac valve calcifications on low-dose unenhanced ungated chest computed tomography: inter-observer and inter-examination reliability, agreement and variability,” *European Radiology* **24**(7), 1557–1564 (2014).